Asian Journal of Pharmaceutical Sciences 17 (2022) 230–240

Available online at www.sciencedirect.com

ScienceDirect

journal homepage: www.elsevier.com/locate/AJPS

Original Research Paper

Metal ions-bridged J-aggregation mediated nanoassembly composition for breast cancer phototherapy

Chen Chen[1], *Shan Yang*[1], *Yufei Liu*, *Yue Qiu*, *Jing Yao*[*]

State Key Laboratory of Natural Medicines and Jiangsu Key Laboratory of Druggability of Biopharmaceuticals, Department of Pharmaceutics, China Pharmaceutical University, Nanjing 211198, China

ARTICLE INFO

Article history:
Received 22 October 2021
Revised 27 November 2021
Accepted 11 January 2022
Available online 25 February 2022

Keywords:
Metal ions
J-aggregates
Combination therapy

ABSTRACT

Recently, the highly ordered J-aggregates of organic dyes with intriguing optical properties have received considerable attention in biomedical applications. Herein, binary metal ions Mn(II)/Fe(III) are used to induce the formation of indocyanine green (ICG) J-aggregates. Further, the sheet-like J-aggregates are able to act as "carriers" for loading hydrophobic chemotherapeutic gambogic acid (GA), realizing the effect of "killing two birds with one stone" for both treatment and delivery. The as-designed nanoassembly is formed spontaneously in aqueous environment *via* π-π stacking, electrostatic interaction, and hydrophobic force, exhibiting enhanced photostability of ICG and outstanding reactive oxygen species (ROS) generation ability. Moreover, significant inhibition of tumor growth by the synergetic effect of phototherapy and chemotherapy is verified in a subcutaneous 4T1 tumors model. In conclusion, this work not only presents a facile and green approach to manufacture carrier-free nanodrugs, but also establishes a universal platform that has potential application in the co-delivery of near-infrared dye and hydrophobic molecules.

1. Introduction

The photodynamic therapy (PDT) as an efficient anti-tumor strategy has been proved to be suitable for breast cancer by preliminary clinical trials [1,2]. Compared with surgical resection, its non-invasiveness, low side effects and high treatment efficiency are beneficial to improve the compliance of breast cancer patients. Indocyanine green (ICG) is the only near-infrared dye approved by FDA and displays great potential in anti-tumor phototherapy. Under 808 nm laser irradiation, ICG can convert absorbed near-infrared laser energy to heat for photothermal therapy (PTT) and to cytotoxic reactive oxygen species (ROS) for PDT [3,4]. ICG is able to assemble with various ingredients (e.g., peptides, proteins, small molecules) *via* π-π stacking, electrostatic interactions, and hydrophilic/hydrophobic interactions [5], caused by its

* Corresponding author.
E-mail address: yaojing@cpu.edu.cn (J. Yao).
[1] These authors contributed equally to this work.
Peer review under responsibility of Shenyang Pharmaceutical University.

https://doi.org/10.1016/j.ajps.2022.01.003

unique structure, which comprises both lipophilic polycyclic moieties and hydrophilic sulfonate groups [6]. Such an ICG-based co-assembly strategy can not only meet the demands of different therapeutic purposes but also overcome the disadvantages of photo-degradation and low tissue-selectivity of ICG [7–9]. However, the co-assembled nanodrugs are unstable because of insufficient interactions [10]. Herein, we conceive a carrier-free nanodrug by co-assembling of ICG and a chemotherapeutic agent with the aid of metal ions to strengthen the intermolecular interactions, and meanwhile achieve the synergistic phototherapy and chemotherapy. Gambogic acid (GA), a natural compound isolated from gamboge, is selected as the chemotherapeutic agent. GA has a significant anti-tumor effect on a wide variety of solid tumors due to its efficient apoptosis-inducing activity [11]. Furthermore, GA can improve the PTT effect through inhibiting 90-kDa heat shock protein [12].

J-aggregates of highly ordered molecular arrangement are specific organic dye supramolecular assemblies [13,14]. Such aggregates are characterized by typical red-shifted absorption [15,16], low radiation transition, and superior resistance to photobleaching [17], which are favorable for phototherapy. J-aggregates could be obtained by encapsulating dye molecules in organic polymers [17,18]. However, this method both raises safety concerns and increases the cost due to the application of synthetic high-molecular-weight polymers. The metal ions were also found to be able to induce J-aggregates of various carbocyanine dyes [19,20]. Notably, Slavnova et al. pointed that ion pairs between monomeric or/and dimeric dyes and metal ions in aqueous solution served as reactants for aggregation [21], indicating that metal ions provided assembly driving forces such as ligand-metal coordination [22] and electrostatic interaction [19]. Furthermore, metal ions can also improve the dielectric constant of the assembly environment [23], which was conducive to the directional aggregation of ICG. Additionally, the low molecular weight of metal ions only occupied a small percentage of the whole nanoassembly, which was superior to high-molecular-weight polymers.

In this case, we constructed a metal ions-bridged J-aggregation mediated nanoassembly through the two-step assembly (Scheme 1). In the first step, ICG self-assembled into J-aggregates (i.e., IFM(J)) in the aqueous environment when induced by binary metal ions, Mn(II) and Fe(III). The obtained J-aggregates displayed sheet-like structure formed by the head-to-tail connection of ICG molecules and could be compressed into spherical and stable nanoassembly by hydrophobic GA in the second step, realizing the co-delivery of the photosensitizer and the chemotherapeutic agent for breast cancer treatment. This assembly behavior could not only overcome the instability of free ICG and the limitations of rapid clearance from the circulation, but also improve the solubility of GA, facilitating the potent of clinic application. It was noteworthy that a trace amount of metal ions was left in the nanoassembly, which avoided the metal toxicity and potential hazards. Upon laser irradiation, IFM-GA generated abundant reactive oxygen species (ROS) both *in vitro* and *in vivo*, demonstrating high PDT efficacy against tumor cells. Furthermore, synergistic enhanced tumor growth suppression effect could be achieved through the combination with GA-mediated chemotherapy, thereby enabling effective tumor-killing under low radiation dose. Such mild temperature phototherapy could be an efficient and safe approach for breast cancer treatment.

2. Materials and methods

2.1. Materials

GA (98.95%) was purchased from Pulis Biological Technology Co., Ltd. (Chengdu, China). ICG (95%), Methylene blue (MB, 95%), and Manganese(II) chloride tetrahydrate ($MnCl_2$•$4H_2O$, 99%) were purchased from Saen Chemical Technology Co., Ltd. (Shanghai, China). Iron(III) chloride hexahdrate ($FeCl_3$•$6H_2O$, ≥ 99.0%) and dimethyl sulfoxide (DMSO, ≥ 99.5%) were purchased from Sinopharm Chemical reagent Co., Ltd. (Shanghai, China). Methanol (≥ 99.5%) was purchased from Yasheng Chemical Co., Ltd. (Wuxi, China). 3-(4,5-dimethyl-2-thiazolyl)−2,5-diphenyltetrazolium bromide (MTT, 98%) was purchased from Aladdin Reagent Database Inc. (Shanghai, China). Fetal bovine serum (FBS) and Dulbecco's modified eagle's medium (DMEM) were purchased from Biological Industries (Israel). Penicillin/streptomycin was purchased from KeyGEN Bio TECH corp. Ltd. (Nanjing, China). Trypsin was purchased from Yifeixue Biotechnology (Nanjing, China). Reactive oxygen species assay kit and tissue mitochondria isolation kit were purchased from Beyotime Biotechnology (Shanghai, China). Other chemicals were of analytical grade.

2.2. Cell culture

4T1 cells were cultured in DMEM medium with 10% (v/v) fetal bovine serum (FBS) and 1% penicillin/streptomycin at 37 °C with 5% CO_2.

2.3. Animal model

BALB/c mice (Female, 5–6 weeks) were bought from Sino-British SIPPR/BK Lab. Animal Ltd. (Shanghai, China). The animal experiments were conducted in conformity to the experimental animal guidelines established by the Animal Center Laboratory of China Pharmaceutical University. 4T1 tumor xenograft model was established as follows: the suspension of 4T1 cells (4×10^6 cells in 100 μl phosphate buffer saline (PBS, 0.01 M) were inoculated under the flank skin of BALB/c mice. The sizes of tumors were calculated as Volume (mm^3) = $a \times b^2 / 2$ (*a*: tumor length; b: tumor width).

2.4. Preparation and characterization of IFM-GA

1.2 mg ICG was dissolved in 4.8 ml water (250 μg/ml), then 800 μl $MnCl_2$•$4H_2O$ aqueous solution (1 mg/ml) and 800 μl $FeCl_3$•$6H_2O$ aqueous solution (1 mg/ml) were added, and stirred for 10 min. The mixture was sonicated for 30 min to obtain IFM(J). Subsequently, 2 ml GA methanol solution (2 mg/ml) was added dropwise into the prepared IFM(J). After stirring for 30 min, the mixture was sonicated for 10 min under ice-water bath, dialyzed (MWCO 3500) against distilled water for 24 h, and centrifuged at 10 000 rpm for 5 min to obtain the supernatant product IFM-GA. The particle size of IFM-GA

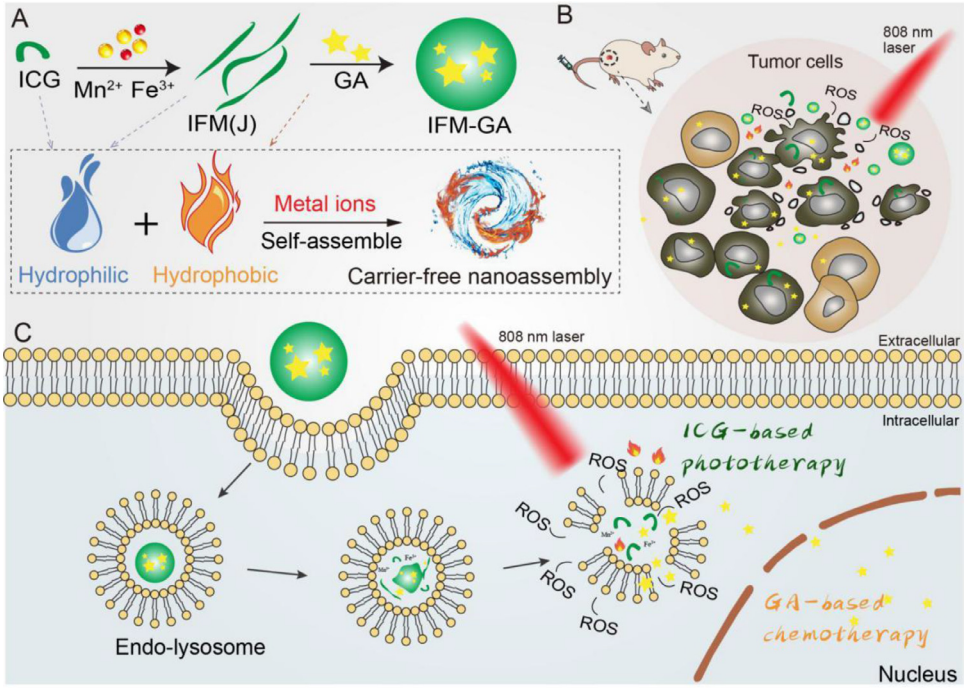

Scheme 1 – Construction (A), therapeutic mechanism (B) and *in vivo* behavior (C) of IFM-GA. IFM-GA were delivered to tumor sites through circulation and released drugs to realize synergistic phototherapy and chemotherapy.

was measured by dynamic light scattering (DLS) instruments (NanoBrook Omni, Brookhaven, USA). Transmission electron microscope (TEM, HITACHI, H-7650) and FTIR (Tensor 27, Bruker Optics, Germany) were used for characterizations of IFM(J) and IFM-GA. The drug loading (DL) and encapsulation efficiency (EE) were calculated as below. The content of ICG and GA was tested with ultraviolet spectrophotometer (TU-1810 PC spectrophotometer, PERCEE, China). The content of Mn(II) and Fe(III) was determined by ICP-MS.

$$\text{DL}\,(\%) = (\text{weight of drug in nanoassembly/total weight of nanoassembly}) \times 100\%;$$

$$\text{EE}\,(\%) = (\text{weight of drug in nanoassembly/weight of initially added drug}) \times 100\%.$$

2.5. *In vitro stability study*

The freshly prepared IFM-GA solution was stored at 4 °C, and the particle size at the time points of 0, 12 h, 24 h, 48 h, 2 weeks, and 2 months were measured.

2.6. *In vitro drug release study*

IFM-GA solution (2 ml) was placed in the dialysis bag (MWCO 3500) and then immersed in a plastic bottle containing 200 ml of 0.5% SDS phosphate buffer of different pH. These bottles were placed on a 37 °C water bath with gentle shaking for 48 h. 1 ml release sample was taken out at 4 h, 8 h, 24 h, and 48 h. Then ethyl acetate was added to extract GA. The GA concentrations in each sample were determined by high-performance liquid chromatography (HPLC) analysis. The mobile phase was methanol-0.1% glacial acetic acid solution (95:5, v/v), and the column temperature was 30 °C. The flow rate was set at 1 ml/min, and the injection volume was 20 µl. The detection wavelength was 360 nm.

2.7. *In vitro photothermal performance*

To evaluate the photothermal effect of IFM-GA, IFM-GA and free ICG solution of equivalent ICG concentration were received 808 nm laser irradiation at a power density of 0.5 or 1 W/cm^2 for 5 min. Water was used as control. In addition, a five-round of on/off laser irradiation at a power density of 1 W/cm^2 was conducted to evaluate the photostability of IFM-GA. The temperature of solutions during laser irradiation were monitored by using a thermal imaging camera (Fluke, USA).

2.8. *In vitro ROS assay*

The ROS generation ability of IFM-GA was measured using MB method. 1 ml ICG or IFM-GA solution of equivalent ICG concentration were mixed with 2 ml MB aqueous solution (8 mg/l), then 1 ml H_2O_2 solution was added, and the mix solutions were irradiated upon 808 nm laser at 0.5 W/cm^2 for 15 min. The absorbance of the mix solutions at the wavelength of 663 nm was measured by ultraviolet spectrophotometer (TU-1810 PC spectrophotometer, PERCEE, China).

The DCFH-DA assay kit was used to evaluate intracellular ROS production. 4T1 cells were inoculated in a 24-well plate (5×10^4 cells per well) for 24 h. Subsequently, different formulations at an equivalent ICG concentration of 1 µg/ml were added. After incubating for 2 h, the drug-containing medium was discarded, and the ROS detection probe DCFH-DA (probe dilution ratio 1:1000) was added. After incubation

in the dark for 20 min, the DCFH-DA probe was removed, and the cells were washed with DMEM and irradiated (808 nm, 0.5 W/cm^2, 5 min). Then, cells were collected for flow cytometry (MACSQuant, Germany) detection of DCF fluorescence intensities.

2.9. Cytotoxicity assay

The cytotoxicity of IFM-GA against 4T1 cells was evaluated by MTT assay. In detail, 5×10^3 4T1 cells per well were seeded in 96-well plates and incubated at 37 °C overnight. Then, free ICG, free GA, IFM(J), and IFM-GA were added. For laser group, the cells were incubated with different formulations for 4 h and then irradiated under 808 nm laser (0.5 W/cm^2) for 5 min. After incubation for another 20 h, 40 μl MTT (2.5 mg/ml) was added and cultured for 4 h. Then, the medium was removed and 150 μl DMSO was added. The optical density (OD) values were measured at 490 nm using a microplate reader (Biotek ELX800, USA).

2.10. In vitro mitochondrial swelling test

To validate the mitochondria damage ability of IFM-GA, the liver mitochondria was obtained from healthy mice using tissue mitochondria separation kit, according to the manufacturer's suggested protocol. The isolated mitochondrial pellet was re-suspended by the stock solution and then incubated with IFM-GA at 37 °C for 20 min. The OD values of these solution at 530 nm was measured by a microplate reader (Biotek ELX800, USA).

2.11. In vivo anti-tumor therapy

BALB/c mice with tumor volume of about 100 mm^3 were randomly divided into different groups. In low dose treatment, on Day 0 and Day 3, mice were intravenously injected with free ICG (1 mg/kg ICG), free GA (2.5 mg/kg GA), IFM(J) (1 mg/kg ICG), IFM-GA (1 mg/kg ICG and 2.5 mg/kg GA) and saline. In standard dose treatment, on Day 0 and Day 3, mice were intravenously injected with free ICG (3 mg/kg ICG), IFM-GA (3 mg/kg ICG and 7.5 mg/kg GA) and saline. For the laser treatment groups, the tumors of mice were irradiated upon 808 nm laser at 0.5 W/cm^2 for 5 min. At last, the mice were euthanized. The major organs were collected for hematoxylin and eosin (H&E) staining. In addition, the tumor sections were stained with ki67.

$$\text{The tumor inhibition rate (\%)} = \left(1 - \text{the average tumor weight of test group/the average tumor weight of control group}\right) \times 100\%.$$

2.12. In vivo ROS assay

The BALB/c mice with tumor volume of about 200 mm^3 were randomly divided into two groups ($n = 3$), and intravenously injected with free ICG or IFM-GA at an equivalent ICG dose of 3 mg/kg. After 6 h, the tumors were pre-injected with DCFH-DA probe (dilution ratio 1:1000) and then irradiated by the 808 nm laser at 0.5 W/cm^2 for 5 min. Then, the tumor tissues were immediately isolated. Frozen sections of tumors were prepared and stained with Hochest 33342 (10 μg/ml) to photograph with an upright fluorescence microscope (Leica DM2500, Germany). Single tumor cell suspension was also prepared for flow cytometer detection (MACSQuant, Germany).

3. Results and discussion

3.1. Preparation and characterization of IFM-GA

The aqueous- and photo-stability of ICG is expected to be improved through the formation of J-aggregates. The fabrication of this carrier-free nanoassembly contained two steps. In the first step, ICG self-assembled into its J-aggregates in the aqueous environment with the aid of Mn(II) and Fe(III) ions. The formation of ICG J-aggregates (i.e., IFM(J)) was confirmed by the appearance of a sharper and red-shifted peak at 890 nm (Fig. 1A). We also noted that the obtained IFM(J) aqueous solution displayed blackish green (Fig. S1). However, the ICG aqueous solution was emerald green, and both the $MnCl_2$ aqueous solution and $FeCl_3$ aqueous solution were colorless. This color-changing phenomenon of IFM(J) suggested that the self-assembly of ICG molecules occurred, which impacted the original chromophores and corresponding dye color. Assembling into J-aggregates by noncovalent interaction could improve the aqueous stability of ICG. As shown in Fig. 1B, a 4.9-fold decrease in the absorption of free ICG was found in aqueous solution at 780 nm after 72 h, while there was little change in IFM(J) group. This change indicated the improved ICG stability after assembly.

In the second step, hydrophobic GA was introduced through the dialysis method, and the final product was obtained in supernatant while the unloaded GA was removed by centrifugation. As shown in Fig. 1C, the as-prepared nanoassembly had a peak of GA at 361 nm, suggesting the incorporation of hydrophobic drug GA. The obtained co-assembly of ICG J-aggregates and chemotherapeutic GA is denoted as IFM-GA. The TEM images (Fig. 1D) revealed that the first step product IFM(J) was mainly sheet-like. Interestingly, the final product IFM-GA displayed spherical with a regular shape and uniform distribution. The particle size of IFM-GA was 101.61 ± 1.80 nm (Fig. 1E), and the polydispersity index (PDI) was 0.105 ± 0.051 measured by DLS method. Also, the DL of ICG and GA were measured to be ~29% and ~70%, while the EE of ICG and GA were approximately 70% and 68%, respectively. The larger particles (> 5 μm) would result in capillary blockade and embolism *in vivo* [24]. Therefore, the particle size and size distribution ought to be closely monitored during storage. As exhibited in Fig. 1F, the particle size of IFM-GA kept at less than 150 nm with PDI of <0.2 during the two-month storage at 4 °C, implying good storage stability of IFM-GA nanoassembly.

3.2. Self-assembly mechanisms study of IFM-GA

To further explore the assembly mechanism of IFM-GA, the force destruction experiment was first conducted to investigate the driving force of assembly. To verify the

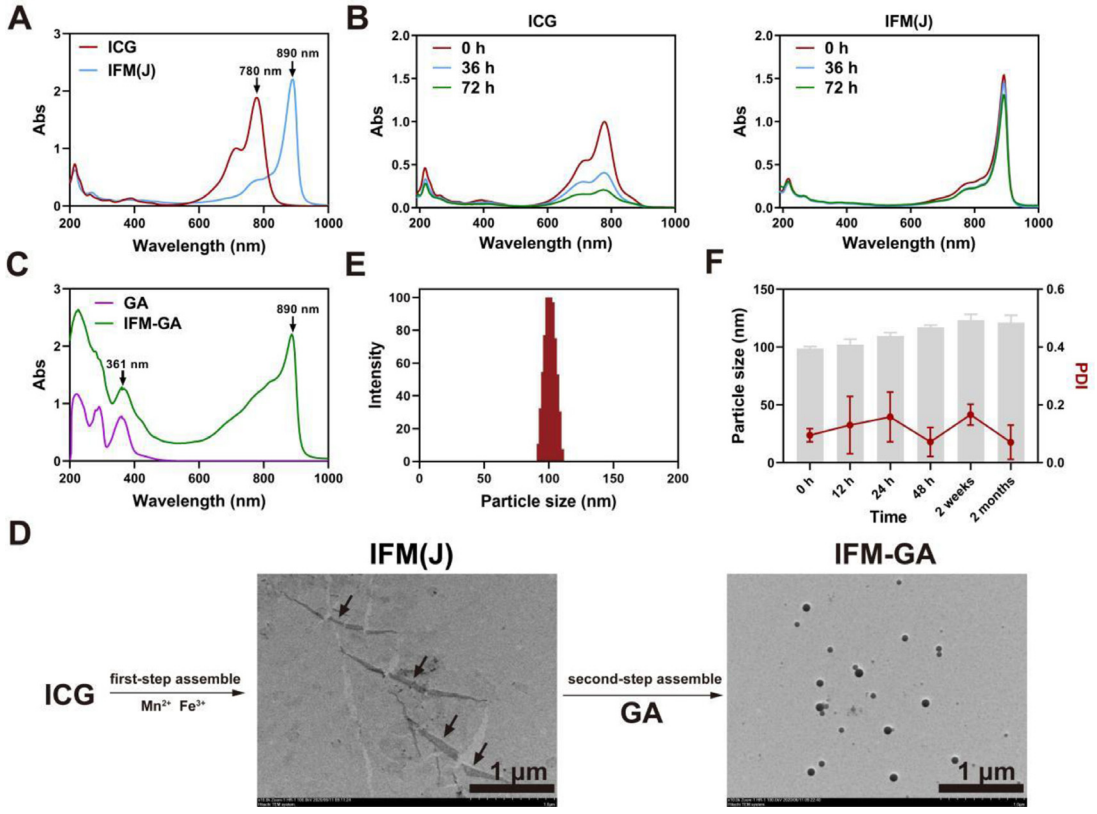

Fig. 1 – (A) The absorption spectra of ICG and IFM(J) solutions. (B) The absorption spectra change of ICG solution and IFM(J) solution within 72 h. (C) The absorption spectra of GA methanol solution and IFM-GA aqueous solution. (D) The representative TEM photograph of IFM(J) and IFM-GA. The black arrows denote IFM(J). (E) The particle size distribution of IFM-GA. (F) The particle size of IFM-GA solution within 2 months stored at 4 °C. Data are presented as mean ± SD ($n = 3$).

existing of hydrophobic force, electrostatic force, and coordination bonds, we added sodium dodecyl sulfate (SDS), NaCl, and ethylenediaminetetraacetic acid (EDTA), respectively, to destroy the intermolecular interactions of the nanoassembly [25]. Once the assembly force was destroyed, the nanoassembly structure became unstable, then reflected in the changes of particle size. After incubation of EDTA and NaCl, IFM-GA was partially disassembled, which exhibited a significant increase in particle size (Fig. 2A) and extremely uneven particle distribution (Fig. S2). With an extended incubation with NaCl and EDTA to 48 h, there was noticeable precipitation, proving the structure of IFM-GA was damaged (Fig. 2B), which demonstrated the existence of electrostatic interaction and coordination interaction in the nanoassembly. Though there was no precipitation seen in the SDS group, the absorption peak of IFM-GA blue shifted to 780 nm (Fig. 2C), owing to the release of ICG from IFM-GA caused by the destruction of the nanoassembly. Hence, we concluded that SDS destroyed the assembly form of IFM-GA to a certain extent, and the hydrophobic interaction also dominated the assembly of IFM-GA.

Metal ions, which are closely related to electrostatic interaction and coordination interaction, together with hydrophobic drugs, which provided hydrophobic interaction, were the key factors in the two-step assembly, so we carried out further investigation into the two-step assembly. First, metal ions were indispensable to the formation of nanoassembly. As shown in Fig. S3, the obtained product displayed similar absorption spectrum as free ICG in the absence of metal ions, which indicated that ICG and GA failed to assemble directly. When only introducing Mn(II), the peak at 890 nm in ICG-Mn-GA disappeared contrast to the ICG-Mn (Fig. S4), and the particle size was hardly measured, suggesting that adding Mn(II) alone couldn't obtain ideal products. When only Fe(III) was introduced, the peak of ICG-Fe at 890 nm disappeared completely after 10 d (Fig. S5), indicating that it was not as stable as IFM(J). Moreover, as shown in Fig. S6, the particle size and PDI of IF-GA significantly increased after 14 d, while IFM-GA nanoassembly remained stable and good monodispersity. These results demonstrated that J-aggregates induced by two kinds of metal ions displayed the best stability, presumably because IFM(J) contained more ICG repeating units, and thus formed a stable "high-dimensional" structure. It was rationally speculated that when two kinds of metal ions existed, the electrostatic interaction and coordination interaction were further strengthened, which might help avoid the disaggregation of J-aggregates.

During the process of second step assembly, these metal ions acted as "bridge" to promote the assembly of ICG and GA, which meant GA replaced the metal ions from ICG J-aggregates. Therefore, there were a small amount of Fe(III) (from 100 μg/ml to 1.31 ± 0.159 μg/ml) and trace Mn(II)

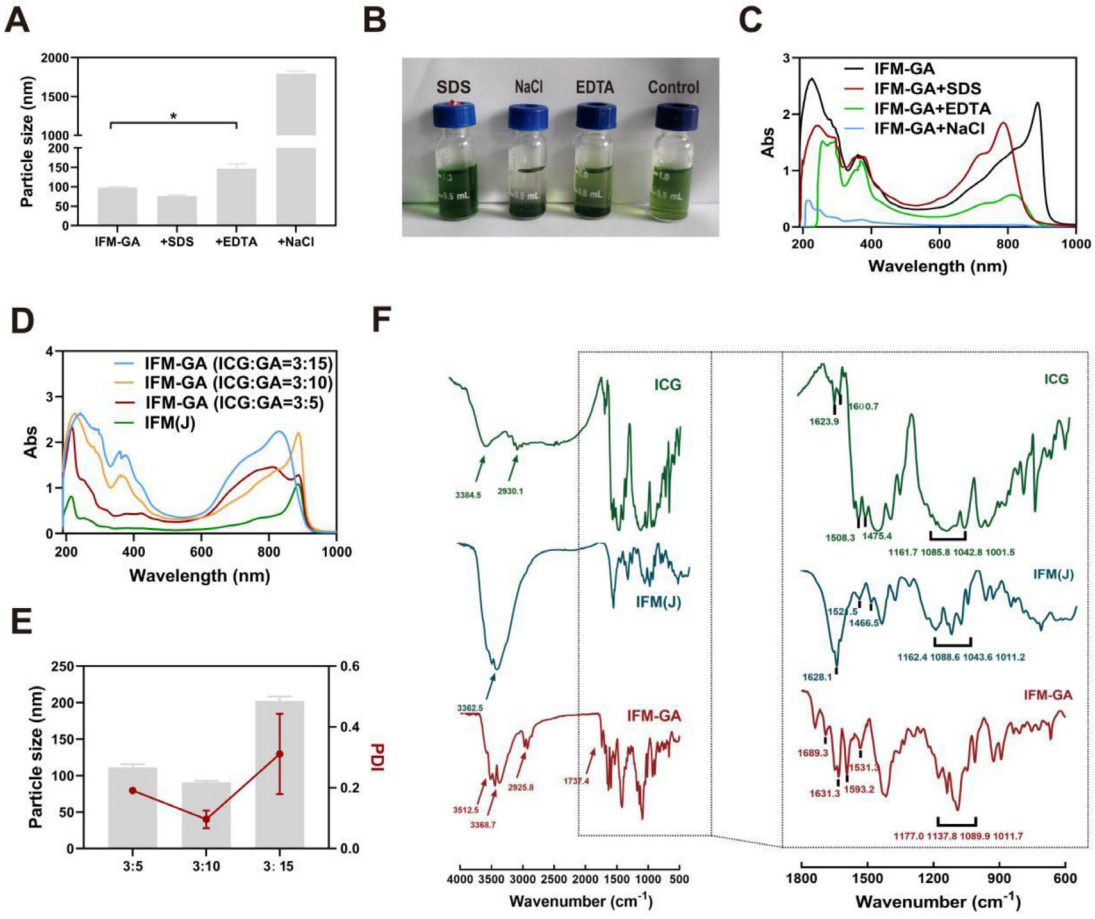

Fig. 2 – (A) The particle size of IFM-GA incubated with SDS, NaCl and EDTA for 0.5 h. Data are presented as mean ± SD ($n = 3$). *$P < 0.05$. (B) The photograph of IFM-GA incubated with SDS, EDTA and NaCl after 48 h. (C) The absorption spectra of IFM-GA incubated with SDS, EDTA (supernatant) and NaCl (supernatant). Spectrum of IFM-GA was also shown in Fig. 1D. (D) The absorption spectra of IFM-GA at ICG:GA ratios of 3:15, 3:10 (also shown in Fig. 1D) and 3:5. (E) The particle size of IFM-GA at different ICG:GA ratios. Data are presented as mean ± SD ($n = 3$). (F) The FTIR spectra of ICG, IFM(J) and IFM-GA.

(from 100 μg/ml to 0.0334 ± 0.0159 μg/ml) left in the final product IFM-GA after second step. Except for electrostatic and coordination interaction, the hydrophobic interaction was also important for IFM-GA assembly. On the one hand, the hydrophobic interaction drove GA to co-assemble with IFM(J) to disperse in the aqueous environment; on the other hand, it kept IFM(J) stable in the dialysis process. Without hydrophobic interaction, the precipitation would be observed in IFM(J) solution during the dialysis process, and the absorption of IFM(J) after dialysis was much weaker than IFM-GA (Fig. S7). Besides, this interaction affected the assembly form, for the absorption spectrum and the particle size of nanoassembly varied with the GA proportion. IFM-GA had an IFM(J) peak at ICG:GA ratio of 3:5 and 3:10, while no IFM(J) peak could be observed at ICG:GA ratio of 3:15 (Fig. 2D). Moreover, IFM-GA displayed satisfying particle size at ICG:GA ratio of 3:10 while showed bigger size with larger PDI at ICG:GA ratio of 3:15 (Fig. 2E). Though the hydrophobic interaction benefited the self-assembly of nanoassmbly, the introduction of excessive hydrophobic molecules might result in unstable assembly, as it limited the IFM(J) to "accommodate" the hydrophobic drug GA. Based on the above results, we adopted the feed ratio of ICG:GA=3:10.

Then, FTIR analysis was used to further explore the assembly mechanism. As shown in Fig. 2F, the characteristic peaks of 3384.5 cm^{-1} and 2930.1 cm^{-1}, that belonged to the ICG side chains, merged to 3362.5 cm^{-1} in IFM(J), for J-aggregates masked the side chain absorption of free ICG. The characteristic peak of 1001.5 cm^{-1} belonged to the ICG sulfonic acid group red shifted to 1011.2 cm^{-1} in IFM(J), which was related to the metal complexation [26]. It suggested that metal coordination was important for the assembly, and the sulfonic acid group of ICG was an important assembly site. In IFM-GA, the peak of 3440.3 cm^{-1} belonged to the GA carboxyl group red shifted to 3512.5 cm^{-1}; the peak of sulfonic acid group further shifted in the second-step compared with IFM(J).

3.3. *In vitro evaluation of IFM-GA*

It is a vital prerequisite for nanoparticles to be stable during circulation after intravenous injection. The stability of IFM-GA was evaluated in 10% serum. As presented in Fig. 3A,

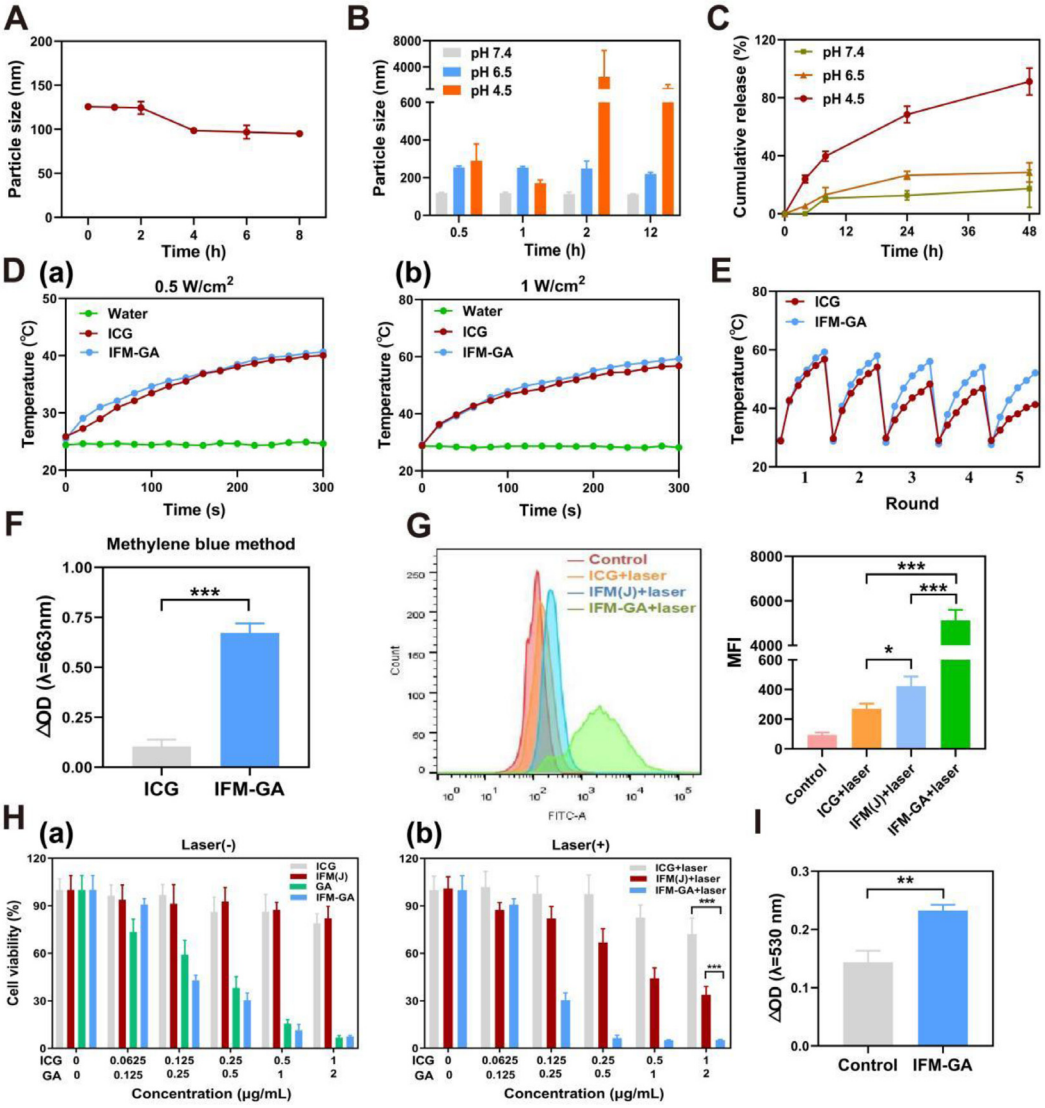

Fig. 3 – (A) The serum stability of IFM-GA within 8 h. Data are presented as mean ± SD ($n = 3$). (B) The particle size of IFM-GA in different pH conditions at different time points. Data are presented as mean ± SD ($n = 3$). (C) The cumulative release of GA from IFM-GA under different pH conditions within 48 h. Data are presented as mean ± SD ($n = 3$). (D) The temperature curves of ICG, IFM-GA and water upon laser irradiation at 0.5 W/cm^2 (a) or 1 W/cm^2 (b). (E) Photothermal stability of ICG and IFM-GA upon five rounds of laser on/off irradiation at 1 W/cm^2. (F) ROS generation of ICG and IFM-GA solution evaluated by MB method. Data are presented as mean ± SD ($n = 3$). (G) Evaluation of intracellular ROS generation of ICG, IFM(J), and IFM-GA by flow cytometry. Data are presented as mean ± SD ($n = 3$). (H) The cell viability of 4T1 treated with different formulations under dark (a) or upon 808 nm laser irradiation at 0.5 W/cm^2 for 5 min (b). Data are presented as mean ± SD ($n = 6$). (I) The change in absorbance at 530 nm of IFM-GA after 30 min incubation with mitochondria. Data are presented as mean ± SD ($n = 3$). *$P < 0.05$, **$P < 0.01$, ***$P < 0.001$.

the particle size of IFM-GA kept stable within 8 h, suggesting that IFM-GA could remain intact in blood circulation, which was beneficial for tumor accumulation. Subsequently, the particle size of IFM-GA was monitored over a period of 12 h under different pH environments (Fig. 3B). In pH 7.4 PBS, which mimicked the pH values of blood circulation, the particle size of IFM-GA remained during the whole monitoring period. However, the particle size of IFM-GA doubled within 0.5 h in pH 6.5 buffer, which simulated the acidic tumor microenvironment, indicating that the assembly of IFM-GA was disturbed. IFM-GA nanoassembly increased to micron size in pH 4.5 buffer, which simulated the acidic environment of the lysosome, implying that its original assembly form was severely destroyed. Consequently, it was speculated that IFM-GA could disassemble in the intracellular lysosome environment.

Then, the GA release behaviors of IFM-GA were further investigated. As shown in Fig. 3C, only 17.39% of GA was released in pH 7.4 PBS at 48 h, suggesting that IFM-GA could avoid the burst release in the blood circulation. A slightly

increased release was found in pH 6.5 with a cumulative release of 28.59% at 48 h. While in pH 4.5, the GA release was much quicker than that in pH 7.4 and 6.5, and the release amount of GA increased notably to 91.15% at 48 h. The above results indicated that the original hydrophobic attraction between IFM(J) and GA could be weakened at a lower pH, for the protonation of GA would lead to greater hydrophilicity [27,28]. Also, IFM-GA would disassemble in an acidic tumor environment once the driving force was diminished and initiated the burst release of GA.

Next, the potential of IFM-GA for phototherapy was studied. The light-to-heat conversion ability of IFM-GA under one round or multiple rounds of irradiation was tested. As shown in Fig. 3D, the temperature of ICG and IFM-GA aqueous solution increased to almost identical levels after a 5-min 808 nm irradiation (0.5 W/cm^2 or 1 W/cm^2), suggesting that the assembly form didn't affect the photothermal conversion effect of ICG. Furthermore, after five cycles of on/off irradiation, the photothermal conversion ability of ICG declined sharply (ΔT from 27.9 °C to 12.3 °C) because of the photobleaching effect, while IFM-GA maintained consistent photothermal conversion ability since the well-structured nanoassembly improved the stability of ICG (Fig. 3E). Moreover, the particle size of IFM-GA remained almost unchanged after five rounds of irradiation (Fig. S8). These data confirmed that IFM-GA had good photostability and could be employed as an effective photothermal agent for anti-tumor PTT.

Adequate generation of cytotoxic ROS is indispensable to tumor PDT. The ROS production of the IFM-GA aqueous solution was evaluated by the MB method. Specifically, the decrease in MB absorbance at 663 nm after irradiation of a solution containing MB and a photosensitizer manifested the consumption of MB, which reflected the level of ROS generation. As can be seen in Fig. 3F, IFM-GA exhibited superiority in ROS generation with a sharp decrease in MB absorbance. Inspired by the result, the intracellular ROS generation of IFM-GA was also evaluated, and DCFH-DA was adopted as the ROS-specific probe. The results from the flow cytometry (Fig. 3G) revealed that ROS generated from IGM-GA was significantly higher than that from free ICG ($P < 0.05$), which might be attributed to the improved stability of ICG aggregates. Moreover, IFM-GA exhibited the strongest ROS generation capability for GA could induce accumulation of ROS and collapse of the intracellular redox balance by inhibiting the enzyme activity of thioredoxin reductase [29].

In addition to enhancing PDT efficacy under irradiation conditions, IFM-GA possessed strong tumor cell killing ability and mitochondrial damage capacity. As shown in Fig. 3H-a, the dark toxicity of IFM-GA against 4T1 cells was significantly higher than that of free ICG and IFM(J), owing to the robust anti-tumor activity of GA. Upon 808 nm laser irradiation, IFM-GA displayed the strongest cytotoxicity with only 5.2% of the 4T1 cells remained alive at an ICG equivalent concentration of 1 μg/ml (Fig. 3H-b). Besides, the calculated combination index (CI) of ICG and GA was 0.8, confirming the good synergistic effect of GA and ICG in IFM-GA (CI<1). It was reported that GA was able to induce mitochondrial injury, and the mitochondrial dysfunction ultimately resulted in cell death [30]. The mitochondria-impairment ability of IFM-GA was confirmed by the mitochondrial swelling test (Fig. 3I).

3.4. *In vivo evaluation of IFM-GA*

PTT utilizes photothermal agents to generate sufficient heat under a near-infrared laser for effective tumor ablation [31]. However, over-heating during laser irradiation may cause inevitable damage to surrounding tissues, and 45 °C is considered the temperature threshold for obvious tissue damage [32]. The injured site would recruit various inflammatory factors, inducing inflammation [33] and stimulating tumor regeneration [34,35], which is not conducive to the patient's treatment compliance and medical prognosis. Therefore, we chose low laser power density (0.5 W/cm^2) to control the tumor temperature of tumor-bearing mice below 45 °C during the treatment and to trigger the PDT simultaneously. As shown in Fig. 4A and B, the group treated with IFM-GA+laser illustrated stronger fluorescence signal than the ICG+laser group in tumor ($P < 0.001$), indicating that IFM-GA efficiently promote the generation of ROS *in vivo*. Therefore, we concluded that IFM-GA would potentially enhance the tumor-killing effect. The anti-tumor effects at the low dose (equivalent ICG dose of 1 mg/kg) were shown in Fig. 4C-a. The group treated with IFM-GA+laser showed slower tumor growth than other groups ($P < 0.01$–0.05). In addition, the strongest tumor growth inhibitory effect was observed in the IFM-GA+laser group, which had a tumor inhibition rate of 43.5% (Fig. 4C-b). It suggested that IFM-GA+laser exhibited obvious therapeutic efficacy *in vivo*, even though the administered dose of ICG was much lower than the widely reported dose (≥ 3 mg/kg) [36–38]. However, the tumors suppression in the IFM-GA+laser group was not satisfying as the relatively fast tumor progression at the end of the treatment. Next, we increased the equivalent dose of ICG to 3 mg/kg. As displayed in Fig. 4C-c and C-d, mice treated with IFM-GA+laser showed the smallest tumor size and the highest tumor inhibition rate (70.0%) among all groups. The tumor volumes of IFM-GA+laser group reduced on Day 5, the day after the 2nd round of treatment, while the tumor volumes of ICG+laser kept increasing, suggesting IFM-GA+laser treatment could shrink the tumor, and ICG+laser failed to retard tumor growth. In addition, the tumors in mice after IFM-GA+laser treatment exhibited a much slower growth rate than the control group ($P < 0.001$) and the ICG+laser group ($P < 0.01$). Of note, complete tumor regression was found in 2 of 5 mice receiving IFM-GA+laser. These results revealed that IFM-GA+laser group exhibited good anti-tumor efficacy. Then, we conducted the ki67 assessment, a test principally used for estimation of cancer prognosis [39]. The results in Fig. 4D showed a significantly lower ki67 expression in the IFM-GA+laser group than other groups, indicating that IFM-GA+laser inhibited the tumor cell proliferation effectively. It would potentially improve the prognosis for breast cancer.

To intuitively analyze the anti-tumor efficacy *in vivo*, we divided the whole anti-tumor therapy into different periods and introduced the relative rumor progression, in turn. Specifically, Day 0–3 and Day 3–6 were designated as periods 1 and 2, respectively. The relative tumor progression was calculated as the average tumor progression volume of the test group during certain period divided by the average tumor progression volume of the control group during the same

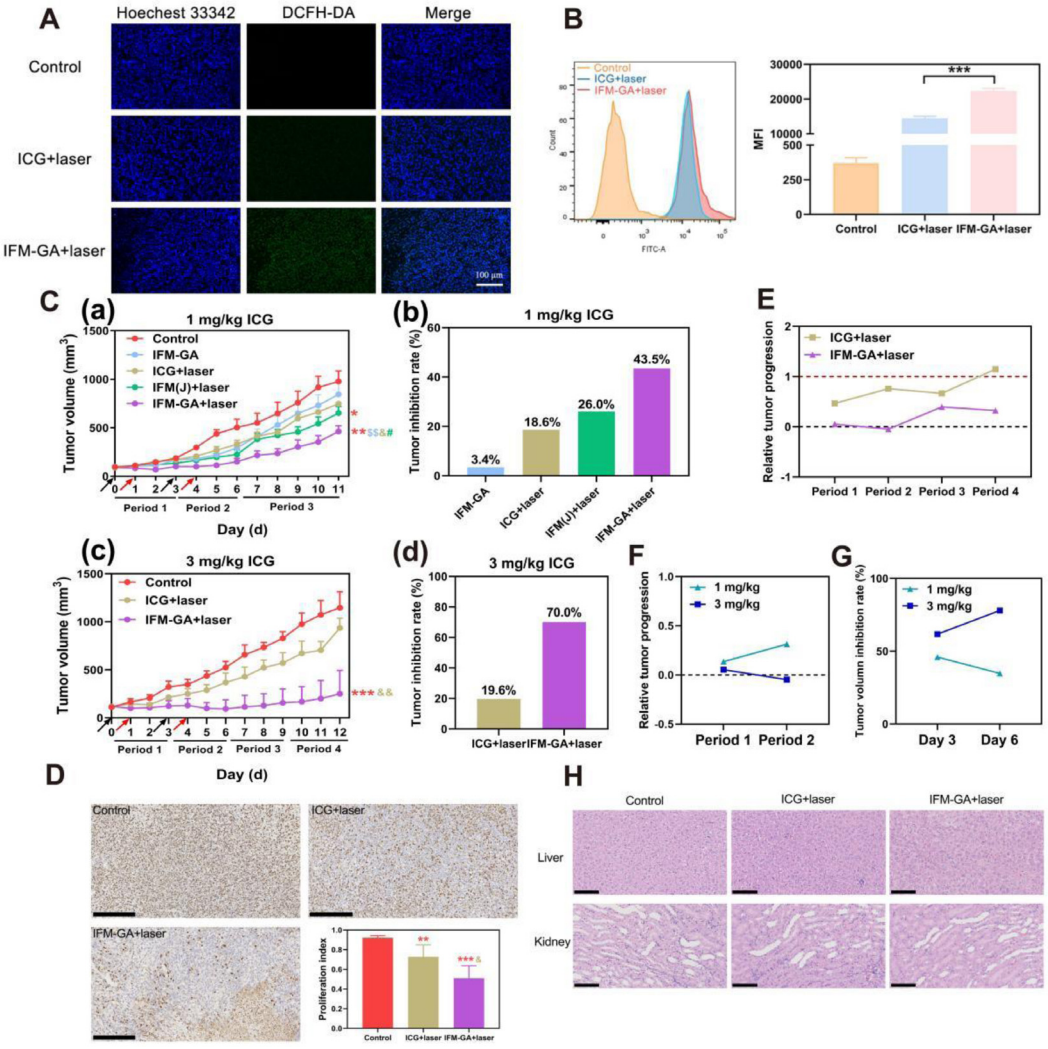

Fig. 4 – (A) Fluorescence images of DCFH-DA stained tumor slices collected from 4T1 tumor-bearing mice for ROS test *in vivo*. (B) Quantification of ROS in 4T1 tumor by flow cytometry. Data are presented as mean ± SD ($n = 3$). ***$P < 0.001$. (C) *In vivo* efficacy of IMF-GA. The tumor growth curves and tumor inhibition rate of 4T1 tumors-bearing mice treated with different formulations at an ICG equivalent dose of 1 mg/kg (a and b) or 3 mg/kg (c and d). The black arrows denote drug injection; the red arrows denote laser irradiation. Data are presented as mean ± SD ($n = 5$). *$P < 0.05$ *vs* control, **$P < 0.01$ *vs* control, ***$P < 0.001$ *vs* control, $^{\$\$}P < 0.01$ *vs* IFM-GA, $^{\&}P < 0.05$ *vs* ICG+laser, $^{\&\&}P < 0.01$ *vs* ICG+laser, $^{\#}P < 0.05$ *vs* IFM(J)+laser. (D) The representative ki67 staining images of tumors and the quantification of ki67 positive rate. Scale bar: 250 μm. Data are presented as mean ± SD ($n = 3$). **$P < 0.01$ *vs* control, ***$P < 0.001$ *vs* control, $^{\&}P < 0.05$ *vs* ICG+laser. (E) The relative tumor progression of different groups. (F) The relative tumor progression of the IFM-GA+laser group at an ICG equivalent dose of 1 mg/kg and 3 mg/kg in two periods. (G) The tumor volume inhibition rates of the IFM-GA group under different doses on Day 3 and Day 6. (H) The representative H&E staining images of livers and kidneys following different treatment. Scale bar: 100 μm.

period. At the standard dose of ICG (Fig. 4E), the tumor inhibition effect of ICG+laser was poor, and the relative tumor progression of period 4 even exceeded 1, indicating that ICG was unable to inhibit tumor growth. In contrast, the relative tumor progression of the IFM-GA+laser group was below 1 in every period, implying better inhibition of tumor growth than the ICG+laser group during the whole treatment. The anti-tumor effects between low dose treatment and standard dose treatment were compared as well. As shown in Fig. 4F, the relative tumor progression of Period 1 was 0.13, while increasing to 0.32 in Period 2 at the low dose ICG (1 mg/kg), indicating that the anti-tumor effect declined, and tumors progressed. In contrast, the relative tumor progression of Period 1 was close to 0 and even lowered to a negative value in period 2 at the standard dose ICG (3 mg/kg), suggesting that the tumor growth was suppressed effectively in both periods and the anti-tumor effect was further enhanced in the second dosing cycle. The tumor volume inhibition rates were consistent with the above relative tumor progression results (Fig. 4G).

In summary, these two studies showed that the IFM-GA nanoassembly, which synergistically combined phototherapy and chemotherapy, could improve the phototherapy effect of ICG under a low-intensity laser (0.5 W/cm^2). Moreover, the therapeutic efficacy of IFM-GA was substantially enhanced when the dose of photosensitizer was increased from 1 mg/kg to 3 mg/kg. Considering the treatment compliance, we monitor the tumor temperature in real-time and set a threshold of 45 °C. During the laser irradiation, the tumor temperature of all the groups did not reach the threshold (Fig. S9), which suggests the excellent patient compliance. In addition, the increased intratumoral temperature might accelerate tissue blood flow [40], thus facilitating the delivery of IFM-GA into tumor, which enhanced the anti-tumor effect of IFM-GA. Therefore, it is beneficial for the IFM-GA+laser group to control the intratumoral temperature in the range of 41–43 °C. Meanwhile, there were no detectable body weight changes during treatment (Fig. S10), and no noticeable pathological changes of the liver and kidney were detected in the H&E staining (Fig. 4H). Moreover, there was no significant differences in serum alanine aminotransferase (ALT), aspartate aminotransferase (AST) and urea nitrogen (BUN) levels between the treatment group and the control group (Fig. S11). These results demonstrated that IFM-GA also caused no significant systemic toxicity.

4. Conclusion

In conclusion, we successfully fabricated the carrier-free nanoassembly IFM-GA based on metal ions-bridged J aggregation. Binary metal ions Mn(II)/Fe(III) which afforded electrostatic and coordination attractions to the negatively charged ICG molecules dominated the formation of ICG J-aggregates. The highly ordered J-aggregates rendered the nanoassembly with favorable properties such as intense NIR-absorptivity, enhanced ROS production capacity, and good photobleaching resistance. Moreover, compared to ICG monomer, the obtained J-aggregates exhibited a more "assemble-available" state, which was conducive to co-assemble with hydrophobic chemotherapeutic GA for synergistic phototherapy/chemotherapy anti-tumor treatment. The results of *in vivo* experiments revealed that IFM-GA nanodrug successfully improved the therapeutic effect of phototherapy under low-dose and low-intensity irradiation conditions. It excavated the photodynamic therapy potential of ICG while avoiding the potential problems of high-intensity irradiation such as hyperthermia-caused injury, providing ideas for further improving breast cancer treatment as well as promoting patient compliance.

Conflicts of interest

The authors declare no conflict of interest.

Acknowledgements

This work was supported by the "333" Project Talent Training Fund of Jiangsu Province (BRA2017432), the Project of Double-top Class Innovation Team (CPU2018GY14), the Project Program of State Key Laboratory of Natural Medicines, China Pharmaceutical University (JKGQ201107) and the Open Project of Jiangsu Key Laboratory of Druggability of Biopharmaceuticals (JKLDBKF201702).

Supplementary materials

Supplementary material associated with this article can be found, in the online version, at doi:10.1016/j.ajps.2022.01.003.

REFERENCES

[1] Baskaran R, Lee J, Yang SG. Clinical development of photodynamic agents and therapeutic applications. Biomater Res 2018;22:25.
[2] Wyss P, Schwarz V, Dobler-Girdziunaite D, Hornung R, Walt H, Degen A, et al. Photodynamic therapy of locoregional breast cancer recurrences using a chlorin-type photosensitizer. Int J Cancer 2001;93(5):720–4.
[3] Bäumler W, Abels C, Karrer S, Weiß T, Messmann H, Landthaler M, et al. Photo-oxidative killing of human colonic cancer cells using indocyanine green and infrared light. Br J Cancer 1999;80(3):360–3.
[4] Philip R, Penzkofer A, Bäumler W, Szeimies RM, Abels C. Absorption and fluorescence spectroscopic investigation of indocyanine green. J Photochem Photobiol A Chem 1996;96(1–3):137–48.
[5] Dai Q, Ren E, Xu D, Zeng Y, Chen C, Liu G. Indocyanine green-based nanodrugs: a portfolio strategy for precision medicine. Prog Nat Sci Mater Int 2020;30(5):577–88.
[6] Lee EH, Lee MK, Lim SJ. Enhanced stability of indocyanine green by encapsulation in zein-phosphatidylcholine hybrid nanoparticles for use in the phototherapy of cancer. Pharmaceutics 2021;13(3).
[7] Zhao R, Zheng G, Fan L, Shen Z, Jiang K, Guo Y, et al. Carrier-free nanodrug by co-assembly of chemotherapeutic agent and photosensitizer for cancer imaging and chemo-photo combination therapy. Acta Biomater 2018;70:197–210.
[8] Guo Y, Jiang K, Shen Z, Zheng G, Fan L, Zhao R, et al. A small molecule nanodrug by self-assembly of dual anticancer drugs and photosensitizer for synergistic near-Infrared cancer theranostics. ACS Appl Mater Interfaces 2017;9(50):43508–19.
[9] Lin J, Li C, Guo Y, Zou J, Wu P, Liao Y, et al. Carrier-free nanodrugs for *in vivo* NIR bioimaging and chemo-photothermal synergistic therapy. J Mater Chem B 2019;7(44):6914–23.
[10] Chen L, Zuo W, Xiao Z, Jin Q, Liu J, Wu L, et al. A carrier-free metal-coordinated dual-photosensitizers nanotheranostic with glutathione-depletion for fluorescence/photoacoustic imaging-guided tumor phototherapy. J Colloid Interface Sci 2021;600:243–55.
[11] Wang P, Jiang F, Chen B, Tang H, Zeng X, Cai D, et al. Bioinspired red blood cell membrane-encapsulated biomimetic nanoconstructs for synergistic and efficacious chemo-photothermal therapy. Colloids Surf B Biointerfaces 2020;189:110842.
[12] Yang L, Hou X, Zhang Y, Wang D, Liu J, Huang F, et al. NIR-activated self-sensitized polymeric micelles for enhanced cancer chemo-photothermal therapy. J Control Release 2021;339:114–29.
[13] Möbius D. Scheibe aggregates. Adv Mater 1995;7(5):437–44.

[14] Fidder H, Knoester J, Wiersma DA. Optical properties of disordered molecular aggregates: a numerical study. J Chem Phys 1991;95(11):7880–90.
[15] Eisfeld A, Briggs JS. The J- and H-bands of organic dye aggregates. Chem Phys 2006;324(2):376–84.
[16] Deng Y, Yuan W, Jia Z, Liu G. H- and J-aggregation of fluorene-based chromophores. J Phys Chem B 2014;118(49):14536–45.
[17] He H., Ji S., He Y., Zhu A., Zou Y., Deng Y., et al. Photoconversion-tunable fluorophore vesicles for wavelength-dependent photoinduced cancer therapy. Adv Mater 201729(19):1606690.
[18] Shao C, Xiao F, Guo H, Yu J, Jin D, Wu C, et al. Utilizing polymer micelle to control dye J-aggregation and enhance its theranostic capability. iScience 2019;22:229–39.
[19] Zhang Y, Xiang J, Tang Y, Xu G, Yan W. Aggregation behaviour of two thiacarbocyanine dyes in aqueous solution. Dyes Pigm 2008;76(1):88–93.
[20] Chibisov AK, Slavnova TD, Görner H. Kinetics of J-aggregation of a thiacarbocyanine dye in aqueous solution: novel aggregate mediated by alcohols and metal ions. Chem Phys Lett 2006;424(4):307–11.
[21] Slavnova TD, Chibisov AK, Görner H. Kinetics of salt-induced J-aggregation of cyanine dyes. J Phys Chem A 2005;109(21):4758–65.
[22] Huang X, Zhao F, Li Z, Tang Y, Zhang F, Tung CH. Self-assembled nanowire networks of aryloxy zinc phthalocyanines based on Zn−O coordination. Langmuir 2007;23(9):5167–72.
[23] Guan AJ, Zhang JT, Wang LX, Cui J, Xiang JF, Sun X, et al. Spontaneous formation and reversible transformation between achiral J- and chiral H-aggregates of cyanine dye MTC. RSC Adv 2019;9(20):11365–8.
[24] Wu L, Zhang J, Watanabe W. Physical and chemical stability of drug nanoparticles. Adv Drug Deli Rev 2011;63(6):456–69.
[25] Xiong H, Wang Z, Wang C, Yao J. Transforming complexity to simplicity: protein-like nanotransformer for improving tumor drug delivery programmatically. Nano Lett 2020;20(3):1781–90.
[26] Chu C, Ren E, Zhang Y, Yu J, Lin H, Pang X, et al. Zinc(II)-dipicolylamine coordination nanotheranostics: toward synergistic nanomedicine by combined photo/Gene therapy. Angew Chem Int Ed 2019;58:269–72.
[27] Zhang J, Li J, Shi Z, Yang Y, Xie X, Lee SM, et al. pH-sensitive polymeric nanoparticles for co-delivery of doxorubicin and curcumin to treat cancer via enhanced pro-apoptotic and anti-angiogenic activities. Acta Biomater 2017;58:349–64.
[28] Ramasamy T, Ruttala HB, Chitrapriya N, Poudal BK, Choi JY, Kim ST, et al. Engineering of cell microenvironment-responsive polypeptide nanovehicle co-encapsulating a synergistic combination of small molecules for effective chemotherapy in solid tumors. Acta Biomater 2017;48:131–43.
[29] Duan D, Zhang B, Yao J, Liu Y, Sun J, Ge C, et al. Gambogic acid induces apoptosis in hepatocellular carcinoma SMMC-7721 cells by targeting cytosolic thioredoxin reductase. Free Radic Biol Med 2014;69:15–25.
[30] Guizzunti G, Batova A, Chantarasriwong O, Dakanali M, Theodorakis EA. Subcellular localization and activity of gambogic acid. Chembiochem 2012;13(8):1191–8.
[31] Hu JJ, Cheng YJ, Zhang XZ. Recent advances in nanomaterials for enhanced photothermal therapy of tumors. Nanoscale 2018;10(48):22657–72.
[32] Lu N, Huang P, Fan W, Wang Z, Liu Y, Wang S, et al. Tri-stimuli-responsive biodegradable theranostics for mild hyperthermia enhanced chemotherapy. Biomaterials 2017;126:39–48.
[33] Pan W, Zhang X, Gao P, Li N, Tang B. An anti-inflammatory nanoagent for tumor-targeted photothermal therapy. Chem. Commun. 2019;55(65):9645–8.
[34] Zhang L, Zhang Y, Xue Y, Wu Y, Wang Q, Xue L, et al. Transforming weakness into strength: photothermal-therapy-induced inflammation enhanced cytopharmaceutical chemotherapy as a combination anticancer treatment. Adv Mater 2019;31(5):1805936.
[35] Dong Q, Wang X, Hu X, Xiao L, Zhang L, Song L, et al. Simultaneous application of photothermal therapy and an anti-inflammatory prodrug using pyrene–aspirin-loaded gold nanorod graphitic nanocapsules. Angew Chem Int Ed 2018;57(1):177–81.
[36] Wang Y, Xie Y, Li J, Peng ZH, Sheinin Y, Zhou J, et al. Tumor-penetrating nanoparticles for enhanced anticancer activity of combined photodynamic and hypoxia-activated therapy. ACS Nano 2017;11(2):2227–38.
[37] Chen Q, Liang C, Wang C, Liu Z. An imagable and photothermal "Abraxane-like" nanodrug for combination cancer therapy to treat subcutaneous and metastatic breast tumors. Adv Mater 2015;27(5):903–10.
[38] Song S, Shen H, Yang T, Wang L, Fu H, Chen H, et al. Indocyanine green loaded magnetic carbon nanoparticles for near infrared fluorescence/magnetic resonance dual-modal imaging and photothermal therapy of tumor. ACS Appl Mater Interfaces 2017;9(11):9484–95.
[39] Davey MG, Hynes SO, Kerin MJ, Miller N, Lowery AJ. Ki-67 as a Prognostic Biomarker in invasive breast cancer. Cancers 2021;13(17):4455 (Basel).
[40] Urano M, Kuroda M, Nishimura Y. For the clinical application of thermochemotherapy given at mild temperatures. Int J Hyperthermia 1999;15(2):79–107.